Composites & nanocomposites

Effect of carbon enrichment in polymer-derived ceramers on the electrochemical characteristics of their derived carbons

A. Tamayo[1],* , Mª. A. Rodriguez[2], J. Rubio[1], and F. Rubio[1]

[1] *CSIC, Institute of Ceramics and Glass, Spanish National Research Council, Kelsen 5, 28049 Madrid, Spain*
[2] *University of Extremadura, Avda Elvas S/N. 06006, Badajoz, Spain*

ABSTRACT

The synthesis of C-rich ceramers from a commercial polycarbosilane has been realized through the incorporation of divinylbenzene (DVB) to the polymer SMP-10. After pyrolysis, the obtained ceramers were dry etched to produce highly porous carbide-derived carbons (CDCs). The excess carbon was segregated in the form of amorphous carbon out from the ceramer matrix. The resulting CDCs possess a carbon nanocrystallite size which turns to be independent on the DVB incorporated or the pyrolysis and chlorination temperature. The electrochemical characterization reveals that the consolidation of the ceramer or ceramic network leads to a reduction of the carbon heterogeneities, thus improving its electric conductivity. When the ceramic network is formed, the behavior of the CDC as electrode supercapacitor is optimized and turns to be independent on the amount of DVB incorporated.

Springer

GRAPHICAL ABSTRACT
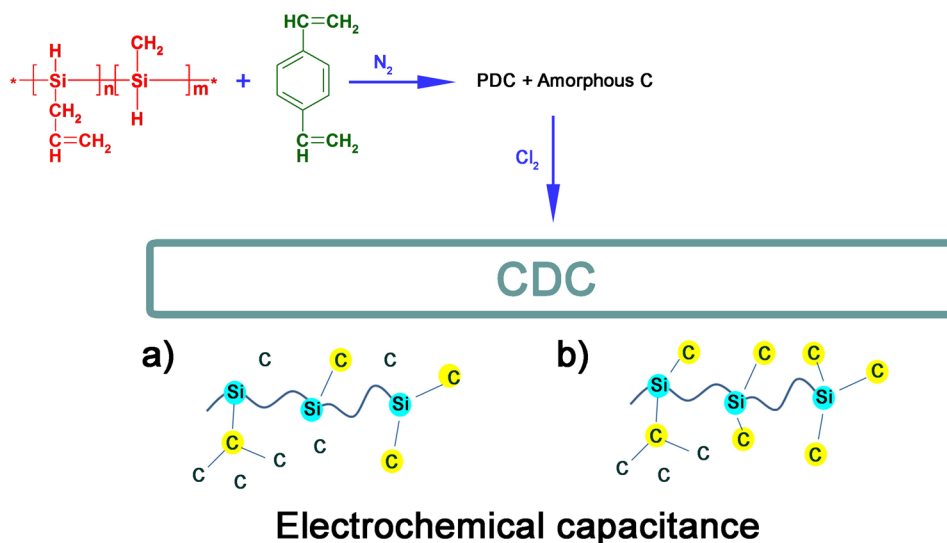
Introduction

Self-templating methods are well-developed strategies to produce highly porous carbon with diverse porous structures with tailored morphology for capacitor electrodes [1, 2]. In general, porous carbons with poor mesopore arrangement are the less desirable choice since they show slow mass transport due to the long and tortuous mesopores which may hinder the transfer of electron and ion into the inner pores. Block copolymers used together with thermosetting resins allow the obtaining of complex carbon nanostructures which, after an activation process, contain cylinder and gyroid pores [3]. Tunable pore nanoarchitectures in terms of pore volume and surface areas are also obtained in metalorganic frameworks (MOF)-derived carbons [4]. Their almost endless combinations of organic and inorganic constituents for producing by MOFs simple coordination chemistry make them highly attractive for many technological applications [4]. Despite the large amount of investigations in MOFs, there is still room to design new carbon materials by adjusting the reacting conditions such as solvent environments, temperature, pH, and reaction time [5]; however, the high cost of precursors, the complex protocols, and, from the practical point of view, the low volumetric energy density are the main difficulties for these class of materials to reach the commercial state.

The carbide-derived carbons (CDCs) are a class of carbon materials produced from a self-templating method with a wide variety of functionalities, edge terminations, stacking order, graphitization which can be selected by the appropriate choice of the metal atom in the primary carbide and the synthesis temperature [6–10]. The type of etchant [11, 12] as well as the etching temperature [13, 14] and post-synthesis treatments [15, 16] has been widely studied aiming to stablish the most optimal parameters for achieving a tunable morphology. The polymer-derived ceramic (PDC) route has been proved to be a feasible strategy to obtain ceramics based in SiC which can be further etched to obtain highly porous carbonaceous and CDC materials [17]. Typically, silicon-based polymers are used as precursors of PDCs being the structure and composition of the resulting ceramic primarily affected by the pyrolysis conditions and the preceramic polymer used [10]. The most common preceramic polymers used for obtaining SiC are polycarbosilanes (PC), which evolve to a ceramic materials through several steps: (i) loss of low molecular mass components at temperatures below 200–400 °C, (ii) organic to inorganic transition, leading to amorphous silicon carbide or ceramers, occurring at intermediate pyrolysis temperature, and (iii) conversion of amorphous to crystalline silicon carbide when the pyrolysis temperature exceeds 1000 °C. In addition, it is a common feature of the materials processed by the PDC route, the presence of a carbon excess that undergoes through phase separation, and is identified as "C_{free}" [18]. One of the main advantages of this method is the easiness of manufacturing

since it takes the advantage of starting from a polymer precursor to process custom-shaped materials such as fibers, coatings, and self-supported films. Polycarbosilanes can be turned into fibers by electrospinning, and the CDC fibers can be used as self-supporting fiber films electrodes with higher capacitance and high power handling ability compared with electrodes with binder-added electrodes [19].

The addition of divinylbenzene (DVB) to a polycarbosilane (PCS) is known to increase the cross-linking degree of the preceramic network; however, its ceramic yield is only limited to a little amount, since the increased cross-linking is not compensated with the high weight loss occurring during the thermal conversion and promoted by the DVB [20]. By tuning the amount of DVB incorporated to the preceramic network, there can be prepared materials with different crystallinities [21] as well as different porous structures because of the modification of the reactions involved in the pore formation [22].

Duan et al. explored the PDC route for the obtaining of CDC [23, 24]. They prepared highly crystalline SiC from a polysiloxane subjected to a carbothermal reduction at 1500 °C and then they proceed to a chlorine etching at temperatures comprised between 600 and 900 °C. The obtained CDC samples were all micro-mesoporous with SSA over 2000 m^2/g and where the carbon ordering decreased as the etching temperature was raised [23]. When a ceramer was used instead of a crystalline SiC, they observed that the C phase was developed by means of the chlorination process although no crystalline SiC was previously nucleated. In this case, the increase in the etching temperature leads to an increase in the carbon ordering [14]. Some other methods for obtaining CDC out from SiC materials are based on electrochemical etching, which uses molten salts as etching agent and allow obtaining SSA as high as 900 m^2/g [25] and heat treatment with molten alkaline compounds [26].

Oschatz et al. used the traditional sacrificial template technique to prepare CDC from a mixture of PCS and DVB and obtained significantly higher total pore volumes and specific surface areas (SSA) compared to the materials synthesized in the absence of DVB [27]. Similarly, studies carried out in CDC capacitor electrodes containing high surface area nanospheres synthesized from PC and DVB show that the energy density provided by the tested assemblies was maximized at low DVB/PCS ratio because of the higher pore accessibility and better flow characteristics [28].

Perez-Roman et al. [29] varied the amount of DVB incorporated to the preceramic network and obtained different interconnectivity among the SiO_2 and SiC units in the pyrolyzed material and corroborated the observations of Sorarù et al. [30] who demonstrated that the differences in the network cross-linking lead to a differentiated lability of the SiO_2 and SiC species toward halogen etching.

In this work, we have prepared SiC materials from a preceramic polymer where the amount of DVB incorporated varied from 1 to 20% in weight thus obtaining CDC materials with different pore structures and connectivity. The structural characterization of the obtained CDC revealed that there is major network connectivity as the pyrolysis temperature increases which is translated in more Si–C mixed bonds. Despite of the more amount of C incorporated, there are almost no differences in the in-plane correlation length of the carbon nanodomain size of the CDC materials independently on the chlorination temperature and the DVB content as well. It was proved that the excess carbon is expelled out from the ceramer matrix as amorphous carbon that during the chlorination process suffers almost no variation. The main difference encountered is the increase in the curvature degree of the C surface occurring as the chlorination temperature and the DVB content were raised. At the highest treatment temperature, the ceramer matrix was consolidated, thus leading to the obtaining of CDC with excellent conductivity and performance characteristics suitable for being used as electrodes in EDLCs.

Experimental

The ceramer samples were synthesized from a commercially available liquid polycarbosilane (AHPCS SMP-10® Starfire Systems, USA) mixed with different amounts of divinylbenzene (DVB, Sigma-Aldrich) in a dry box to avoid oxygen and moisture contamination. Tetrahydrofurane (THF, Merck) was used as the solvent for the complete dissolution of the components. After 1h stirring at RT, the solvent was eliminated under vacuum and then the dried mixtures were pyrolyzed in an alumina tube furnace under a continuous nitrogen flow of 150 ml/min. The heating/cooling rate was fixed to 5 °C/min, and the temperatures of the treatment were 600—900 °C (2h dwelling after 5 h at 280 °C). The chlorination treatment was carried out at the same temperature as the pyrolysis by maintaining

for 2 h the maximum temperature under a continuous Cl_2/N_2 flow of 80 ml/min in a 90/10 ratio.

The infrared spectra (FTIR-ATR) were obtained by an FTIR instrument (PerkinElmer, Spectrum BX) working in the ATR (attenuated total reflectance) mode. The Raman spectroscopy was performed in a Renishaw InVia spectrophotometer by using the 514 nm Ar^+ ion laser as excitation source in the confocal mode. The spectra were the accumulated signal of 10 collections with an acquisition time of 10 s. X-ray diffraction patterns were obtained by employing a Bruker D8 Advance diffractometer using Cu $K_{\alpha1}$ (1.540598 A) radiation and operating at 40 kV. Simultaneous thermogravimetric analysis (TGA) and differential thermal analysis (DTA) were performed in a TA Instruments SDT Q600 heating the samples at 1000 °C at a constant heating rate of 10 °C/min and 100 ml/min air or N_2 flow. The microstructure of the CDC materials was observed by a Scanning Electron Microscope (FE-SEM, Hitachi 4700-S) operating at 20keV and by High-Resolution Transmission Electron Microscope (HR-TEM, JEOL 2100 F, JEOL Ltd., Japan) operating at 200 kV. Finely grinded particles were dispersed ethanol and then dropped onto a lacey carbon supported copper grid. N_2 adsorption–desorption isotherms were obtained in a Tristar Equipment (Micromeritics, USA) after degassing at 120 °C overnight. The chemical composition of the CDC materials was obtained by LECO elemental analyzers, RC-412 for hydrogen, TC-500 for oxygen and CS-200 for carbon.

The electrochemical performance was evaluated by impedance spectroscopy (EIS) in a PGSTAT204 potentiostat/galvanostat (Metrohm Autolab, B.V., Sweden) using a two electrode setup at room temperature and using 6M KOH as aqueous electrolyte. The electrodes were fabricated by direct deposition over stainless steel current collectors of a slurry containing 10 mg active material plus 5 wt.% polyvinylidene fluoride (PVDF) separated by a glass fiber membrane. (10% n-methyl pyrrolidine was used as dispersion solvent for electrode deposition.) The assemblies were dried at 50 °C overnight and then soaked in 6M KOH for 12 h.

Results

Characterization of the polymer-derived ceramers

Prior to the obtaining of the ceramer-derived carbons (CDCs), the ceramer precursors (which at the same time were obtained from preceramic materials) have been characterized. The FTIR-ATR analyses of these polymer-derived ceramers reveal a significant modification of the structural parameters as a function of the pyrolysis temperature and the amount of DVB incorporated into the preceramic precursors (Fig. 1). The first evidences of the ceramic conversion are well observed in the small peaks located at 1350 and 1246 cm^{-1} which are attributed to Si-CH_2-Si and Si-CH_3 bonds, respectively [31], that progressively disappear when rising the pyrolysis temperature due to the polymer-to-ceramic transformation (Fig. 1a). At 600 °C (Fig. 1b), the peak attributed to the TO mode of the SiC stretching shows a downshift from 798 to 789 cm^{-1} as the DVB content is raised which is attributed to an increased number of dangling bonds in the SiC structure [32]. At this pyrolysis temperature, it is also observed that the relative intensity of the LO mode of the SiC bond (centered at about 970 cm^{-1}) experiments a slight decrease in its relative intensity when the DVB content has increased. The inset in Fig. 1b shows the expected decrease in the band corresponding to the Si–H bond in the AHPCS as the DVB content is raised indicating either hydrosilylation cross-linking between the vinyl group of DVB and the AHPCS Si–H groups or dehydrogenative silylation [20]. No significant differences in the allyl and alkyl bands were appreciated.

When the pyrolysis temperature is increased to 900 °C (Fig. 1c), the SiC structure is more consolidated and now, and the band corresponding to the TO Si–C stretching is shifted to higher wavenumbers as the DVB amount is increased due to the higher C–Si coordination [33]. The observed redshift of the band located at about 800 cm^{-1} is accompanied with an increase in its intensity with the pyrolysis temperature for all the DVB contents (Fig. 1d) as a result of the increased crystallinity of the materials and the formation of a larger amount of mixed Si–C bonds.

The Raman spectra shown in Fig. 2 confirm that at 600 °C, the preceramic structure is not yet transformed to an inorganic material at 600 °C, but by increasing the pyrolysis temperature, the D and G bands characteristic of the carbon-containing materials becomes
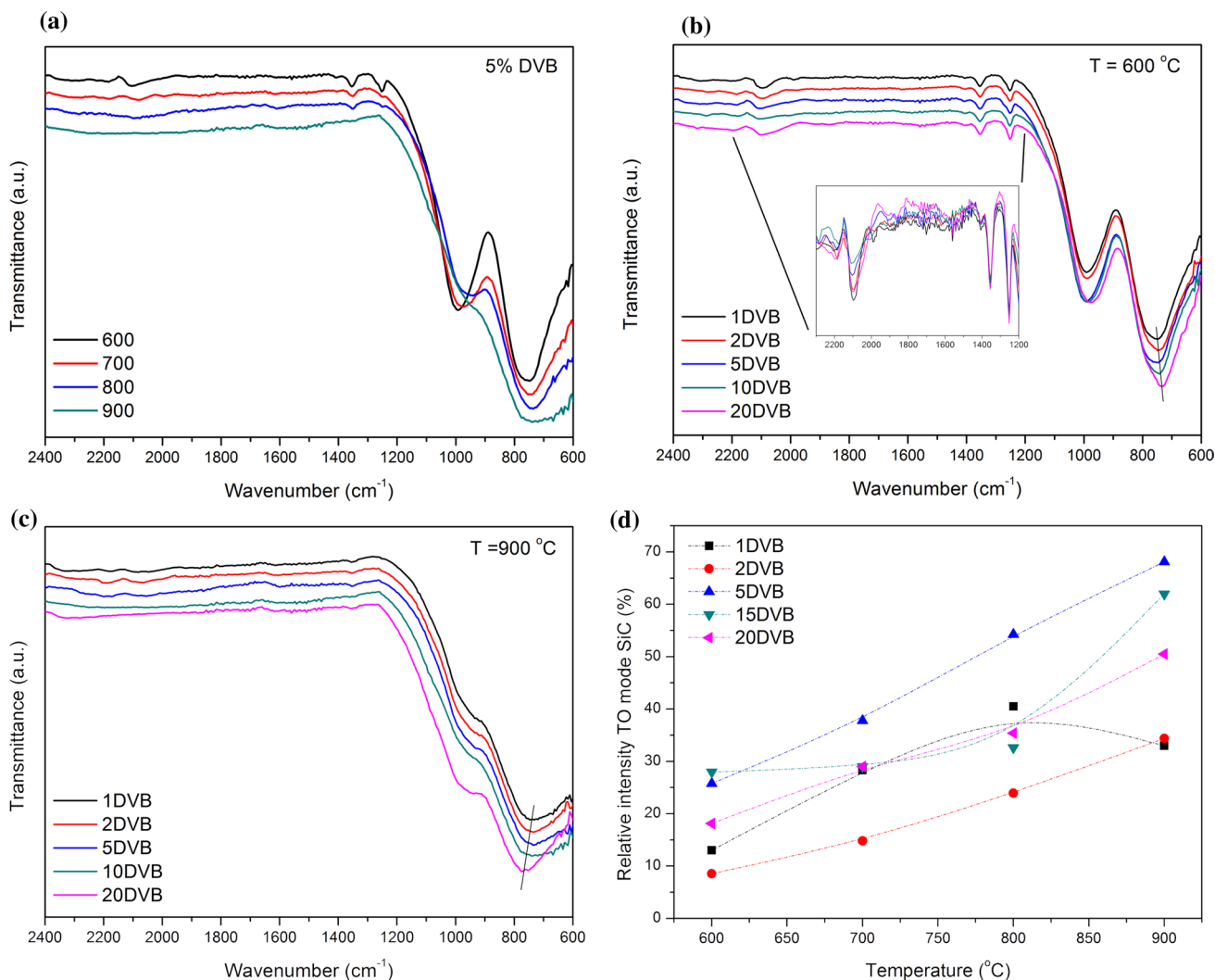
Figure 1 FTIR-ATR spectra of the ceramer samples **a** containing the same amount of DVB and pyrolyzed at different temperatures, **b** pyrolyzed at 600 °C, **c** pyrolyzed at 900 °C, and **d** evolution of the relative intensity of the TO mode of the Si–C stretching as a function of the pyrolysis temperature.

more visible due to the ceramization process and the segregation of the free carbon phase (Fig. 2a). At 600 °C, the most prominent signatures of the spectra correspond to the bending vibrations of the –CH$_2$ and –CH$_3$ moieties of the preceramic polymer and they are revealed as a broad an intense band located around 2870 cm^{-1}. The confocal Raman analysis also evidences the presence of segregated carbon in the form of graphene layers (see inset in Fig. 2a). These graphene layers can be also observed in the samples pyrolyzed at 700 °C, but they were no longer detected in the samples pyrolyzed at higher temperatures.

As shown in Fig. 2a, the characteristic D and G bands located at around 1350 and 1560 cm^{-1} are the common feature in all the spectra of the materials heat treated beyond 700 °C, thus allowing the calculation of the I_D/I_G ratio, that provides information about the ordering degree of the free carbon phase. The evolution of this I_D/I_G ratio with the DVB content at the different pyrolysis temperatures (Fig. 2b) suggests that at the highest temperature, the amount of DVB incorporated into the preceramic material strongly influences the carbon nanodomain size, which in turn depend upon the I_D/I_G ratio, but at intermediate temperatures (i.e. 700 and 800 °C), there is only observed a slight increase if the mentioned ratio.

The differential thermal analyses provide significant information about the evolution of the ceramic
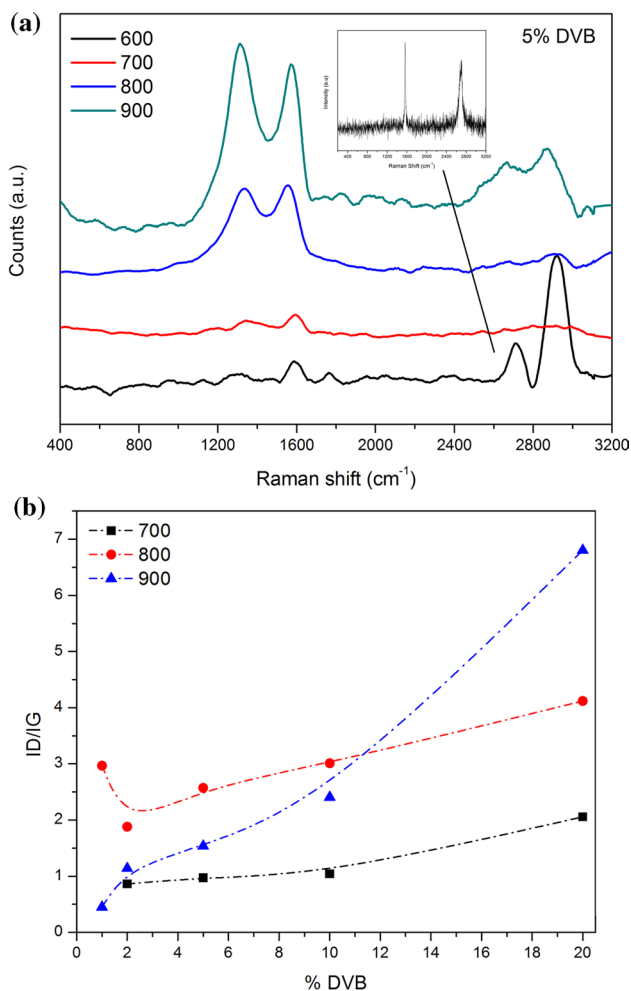
(a)

(b)

Figure 2 Raman spectra of the ceramer samples **a** containing the same amount of DVB and pyrolyzed at different temperatures (the inset shows a detailed Raman spectra of the samples pyrolyzed at 600 °C where the characteristic Raman peaks of graphene are identified) and **b** evolution of the ID/IG ratio as a function of the DVB content.

conversion and the segregation of the carbon phase (Fig. 3). These analyses have been carried out in inert (Fig. 3a, b) and oxidant (Fig. 3 c, d) atmospheres. The endothermic peaks shown in Fig. 3a, b decrease in intensity and shift to higher temperature as the temperature of the treatment is increased and, in the samples subjected to the thermal treatment at the same temperature, as the DVB content is increased, the peak is also slightly shifted to higher temperature values, suggesting that the ceramer network is more thermally stable due to the increased crosslinking promoted by the DVB.

When the analyses were carried out in air atmosphere, the observed exothermic peaks correspond to the oxidation of the carbon phase as well as the SiO_2 formation. By comparing the samples containing 1 and 20%, it is clearly observed that at low DVB contents (Fig. 3c), the oxidation of the materials occurs in less extent than after the incorporation of 20% DVB (Fig. 3c). In addition, as occurred in the analyses carried out in inert atmosphere, for the same amount of DVB, the exothermic peaks shift to higher temperature as the temperature of the thermal treatment is raised and the oxidation is also less likely to occur due to the higher network stability.

Characterization of CDC

After the chlorination treatment carried out to obtain the CDC, the materials were subjected to their corresponding characterization. According to their chemical composition given in Table 1, there are still some silicon remainders in the CDC after chlorination and its content decreases with the temperature of the treatment. The large amount of O and H present in all the materials indicates that the carbon atoms are highly oxidized and contain distinct amounts of functional groups.

All the Raman spectra present the characteristic features of carbonaceous materials (Fig. 4). The spectra have been analyzed and deconvoluted by using a Voigt-shaped function allowing distinguishing the typical bands of the CDC samples named the D* band, appearing between 1150 and 1200 cm^{-1}, the vibration of the A_{1g} mode of the boundaries of graphite or D band which appears at about 1350 cm^{-1}; at 1520 cm^{-1} it is also observed so-called the D'' band which is attributed to amorphous carbon and also to the presence of five- and seven-membered rings linking the aromatic regions. At 1580 and beyond 1600 cm^{-1}, there is also observed the G band, related to the in-plane bond stretching of sp^2 bonds (E_{2g} mode) in carbon clusters and the band commonly labeled D' which is attributed to interactions between the localized vibrational modes of defects in the graphene layers with the extended phonon modes of pure sp^2 carbon [34, 35]. In the second-order Raman spectrum, the G' band near 2650–2710 cm^{-1} (also called the 2D band, since it is the overtone of the D band) arises from a double resonance Raman scattering process mechanism [36] which increases in intensity as the number of graphene layers in the nanocrystallites increases. The D + G band
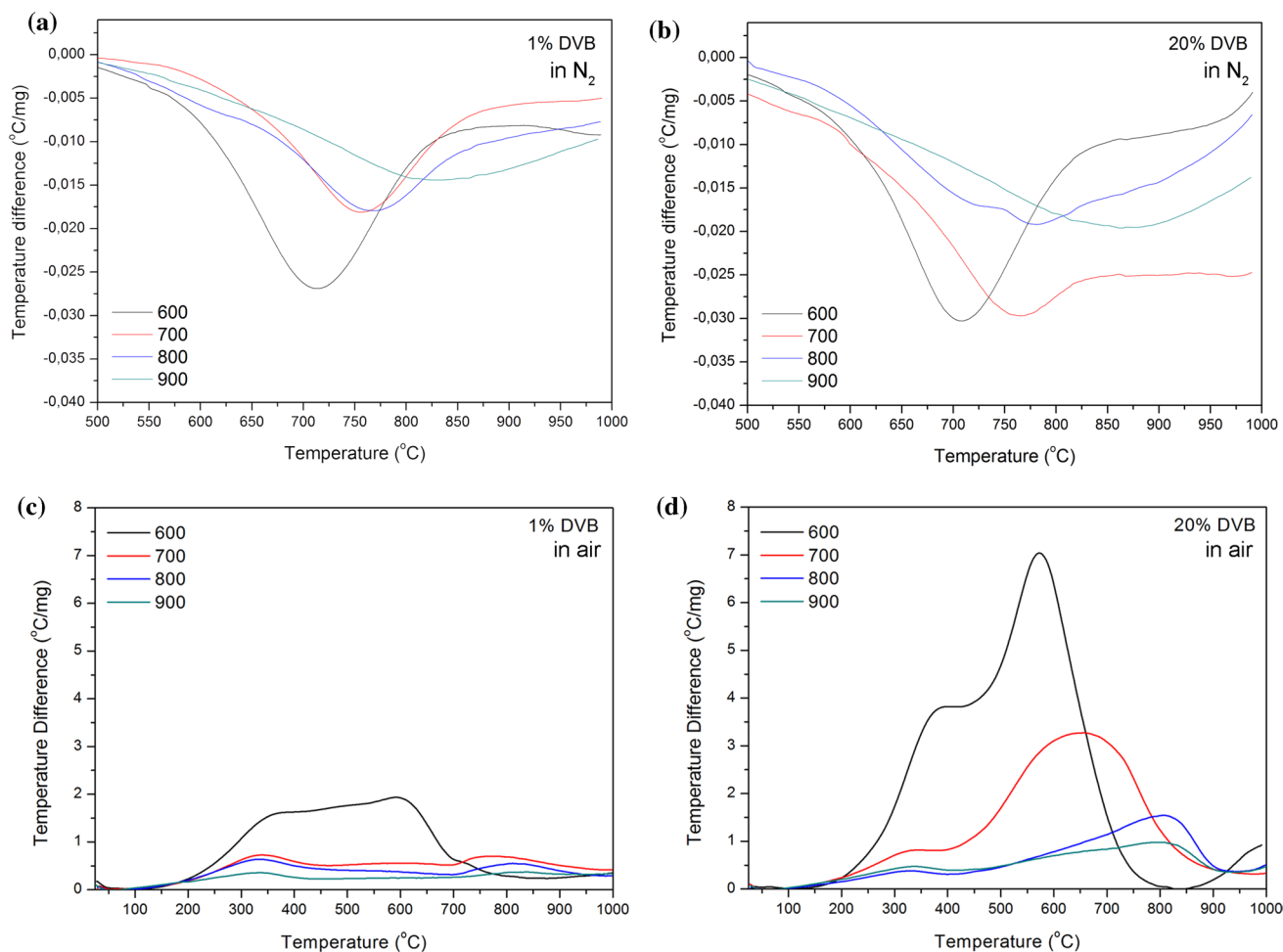
Figure 3 Differential thermal analysis in N_2 atmosphere of the preceramic materials containing **a** 1% DVB and **b** 20% DVB and differential thermal analysis in air atmosphere of the preceramic materials containing, **c** 1% DVB and **d** 20% DVB.

Table 1 Chemical composition of the CDC materials

% DVB	Temperature (^{o}C)			
	600	700	800	900
1	$CO_{0.65}H_{0.35}Si_{0.60}$	$CO_{0.21}H_{0.30}Si_{0.22}$	$CO_{0.20}H_{0.19}Si_{0.07}$	$CO_{0.20}H_{0.18}Si_{0.02}$
2	$CO_{0.57}H_{0.32}Si_{0.52}$	$CO_{0.25}H_{0.37}Si_{0.16}$	$CO_{0.21}H_{0.17}Si_{0.09}$	$CO_{0.26}H_{0.30}Si_{0.12}$
5	$CO_{0.30}H_{0.25}Si_{0.27}$	$CO_{0.23}H_{0.25}Si_{0.18}$	$CO_{0.20}H_{0.18}Si_{0.13}$	$CO_{0.24}H_{0.17}Si_{0.08}$
10	$CO_{0.28}H_{0.09}Si_{0.22}$	$CO_{0.22}H_{0.05}Si_{0.13}$	$CO_{0.26}H_{0.27}Si_{0.15}$	$CO_{0.44}H_{0.42}Si_{0.07}$
20	$CO_{0.25}H_{0.07}Si_{0.18}$	$CO_{0.22}H_{0.04}Si_{0.10}$	$CO_{0.23}H_{0.23}Si_{0.05}$	$CO_{0.23}H_{0.29}Si_{0.05}$

appearing near 2900 cm^{-1} is associated with the presence of defects in the carbon layer [37].

The broadness and position of the bands are indicative of mainly amorphous $sp^2 + sp^3$ carbon, and thus, the I_D/I_G is proportional to L_a^2 (being L_a the average graphene layer extent or the carbon nanodomain size) [38, 39]. There are almost no differences in the L_a values among the samples treated at different temperatures, being the La values comprised between 1.8 and 2.4 nm (Fig. 4b). Notice that 2 nm is the limit of application of the formula used for calculating the L_a. Indeed the most significant differences are
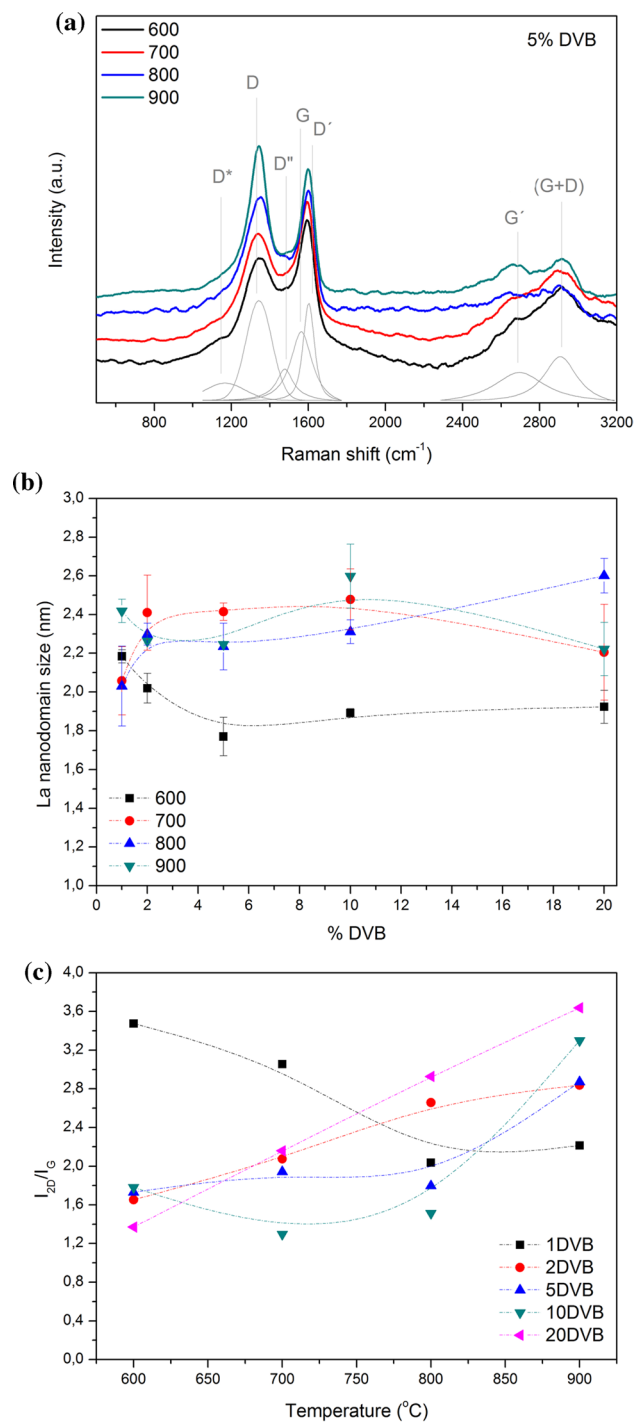
Figure 4 **a** Raman spectra of the CDC materials containing 5% DVB at different chlorination temperatures, **b** La carbon nanodomain size as a function of the DVB amount in the CDC material and **c** evolution of the 2D/G intensity ratio with the chlorination temperature.
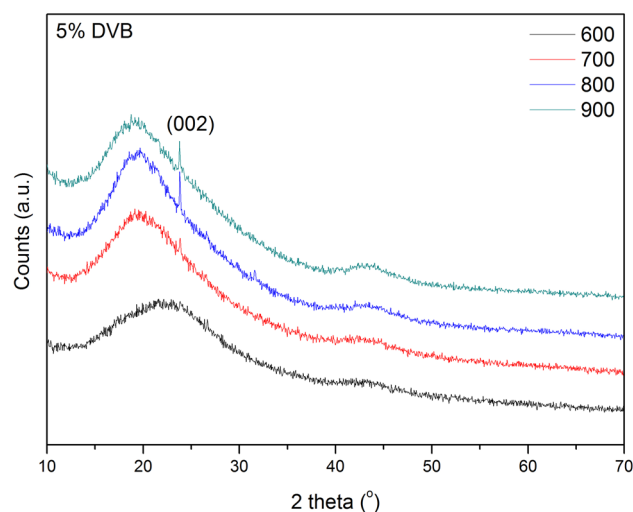
Figure 5 XRD patterns of the CDC containing 5% DVB at different chlorination temperatures.

found in the second-order Raman spectrum, which becomes more resolved as the chlorination temperature increases. The 2D band at about 2650–2710 cm^{-1} is the overtone of the D band, and it is active because of the momentum conservation of two phonons generated at the *K* symmetry point in the Brillouin zone having equal and opposite wavevectors. In graphitized samples, it is generally accepted that the second-order spectrum serves as an estimation of their degree of graphitization. High 2D/G ratios are characteristic of high-quality graphene with low amount of defects. Figure 4 shows an increase in the 2D/G ratio as the chlorination temperature increases except for the samples containing the lowest amount of DVB indicating more stacking order in the CDC materials obtained at higher temperature and with more DVB added.

The XRD diffractograms (Fig. 5) are characteristic of amorphous materials with two broad features appearing at 2θ angles about 20 and 42. Notice that at low chlorination temperature, the most prominent broad band appears even broader than by increasing the temperature of the thermal treatment and shifted to 2$\theta \approx 22$. In the diffractograms, it is also observed a sharp signal located at 2$\theta = 23.8$ which was attributed to the (002) reflection carbon crystallites sized below 3 nm [40], whereas the second band is attributed to the (004) plane of the disordered carbon structure. The application of the Scherrer [41] equation to the (002) reflection leads to increased *Lc* values

(crystallite size in the prismatic direction) with the increase in the chlorination temperature ranging from 0.3 to 2 nm for the CDC samples obtained at 600 and 900 °C, respectively.

The N$_2$ adsorption isotherms are all of type Ib (Fig. 6a presents the isotherms of the CDC materials containing 5% DVB, and similar isotherms were obtained for the remainder materials), characteristic of a broader range of micropores (< 2 nm) and narrow mesopores (< 2.5 nm). The *SSA* values were determined by fitting the experimental isotherm to Eq. 1

$$V_{ads} = \frac{V_m C_{BET}\left(\frac{P}{P_0}\right)}{\left(1 - \left(\frac{P}{P_0}\right)\right)\left[1 + \left(C_{BET} - 1\right)\left(\frac{P}{P_0}\right)\right]} + V_{mic} \quad (1)$$
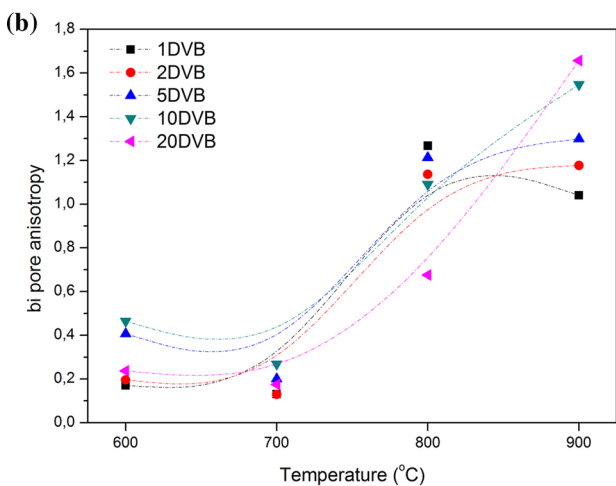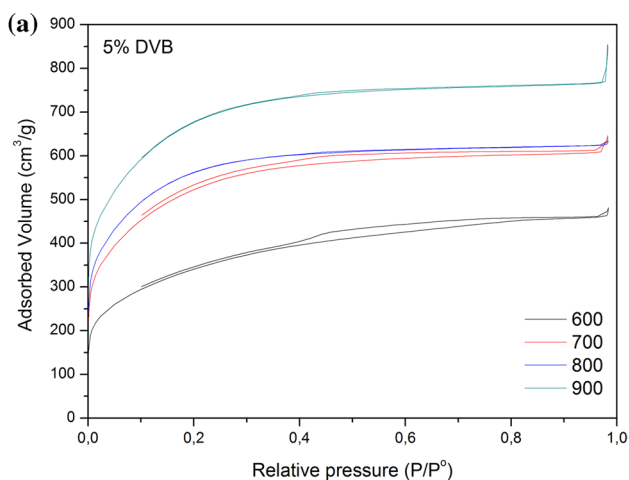
(a) 5% DVB

(b)

Figure 6 **a** N$_2$ adsorption isotherms of the CDC materials containing 5% DVB and **b** anisotropic bi value as a function of the chlorination temperature.

being in this equation V_{ads} the adsorbed volume of N$_2$ on the sample, V_m the adsorbed volume of a N$_2$ monolayer, and V_{mic} the adsorbed volume in micropores. Equation (1) allows calculating the C$_{BET}$ constant at very low P/P_0 values thus avoiding obtaining the negative C$_{BET}$ values that sometimes throws the traditional BET formula when it is applied to highly microporous samples [42]. The calculated SSA values as well as the micropore volume are collected in Table 2.

The *t*-plot method has been also applied to the isotherms to determine the external surface, S_{Ext} [43]. The statistical thickness, *t* (in Å), has been calculated from Eq. (2) by plotting the volume adsorbed versus *t*, being the S_{Ext} the slope of the line at $t \approx 3.5$ Å [44].

$$t = 0.88\left(\frac{P}{P_0}\right) + 6.45\left(\frac{P}{P_0}\right) + 2.98 \quad (2)$$

The micropore area is then calculated from the difference between *SSA* and S_{Ext}, thus allowing calculating the percentage area corresponding to mesopores, % mic, which is also collected in Table 2.

From Table 2, there can be extracted two different behaviors in the CDC materials. The SSA of the materials chlorinated up to 800 °C decreases with the introduction of DVB in the preceramic hybrid, whereas in the case of the samples obtained at 900 °C, there is a maximum in the SSA in the samples containing intermediate amounts of DVB. The V_{mic}, on contrary, decreases as the DVB content increases in the materials obtained at 600 and 700 °C but by increasing the chlorination temperature, this trend is inverted and the V_{mic} increases with the DVB content. This result is also related to the percentage area containing micropores, which increases substantially in the materials obtained at higher temperatures as the DVB content does, but the inverse situation is found in the samples obtained at the lowest temperatures.

The model proposed by Pomonis [45] to calculate the pore anisotropy used the mesoporous region of the N$_2$ adsorption isotherms to calculate the pore anisotropy, b_i. Plotting $\log(S_i^3/V_i^2)$ where S_i and V_i are the surface and volume of pores of radius r_i, as calculated by the application of the BJH method vs $\log(r_i)$ will provide lines with a slope of $(\alpha_i - 1)$ that are used to obtain the pore anisotropies through the application of Eq. (3)

$$b_i = \frac{L_i}{D_i} = 0.5 r_i^{\alpha_i - 1} \quad (3)$$

Table 2 Specific surface area (SSA), micropore volume (Vmic), and percentage area of the total specific surface containing micropores (% mic)

% DVB	Temperature (°C)											
	600			700			800			900		
	SSA (m²/g)	V_{mic} (cm³/g)	% mic	SSA (m²/g)	V_{mic} (cm³/g)	% mic	SSA (m²/g)	V_{mic} (cm³/g)	% mic	SSA (m²/g)	V_{mic} (cm³/g)	% mic
1	1309	288	43	1667	424	50	2309	0	0.1	584	186	10
2	1390	362	34	1219	259	5.9	1324	273	18	1307	300	21
5	645	143	18	1242	262	7.9	1106	255	26	1410	324	22
10	679	157	4.3	1073	233	4.2	1089	300	32	1472	338	37
20	531	124	1.2	890	210	47	1125	326	43	1211	278	87

being L_i and D_i the pore length and pore diameter of pore i, respectively. The obtained bi values are plotted in Fig. 6b. The small bi values presented in the materials obtained at 600 and 700 °C must be attributed to surface roughness, i.e., the length of the pores is quite low with respect of its radius. However, by increasing the temperature, the bi increases significantly, a result that indicates that the mesoporous structure resembles to cylinders. It must be also noticed that at low pyrolysis temperatures, the bi values present minimal variation with the DVB content. At 800 and 900 °C, the dependence of the bi value with the DVB amount is more noticeable, especially in the samples chlorinated at 800 °C, where the bi decreases as the DVB amount is raised. The opposite behavior is encountered in the samples treated at 900 °C, where the pore anisotropy increases with the DVB amount introduced in the preceramic network.

The microstructural characteristics of the obtained materials were also studied by SEM and TEM analyses. The SEM images of the samples containing 5% DVB and heat treated at different temperatures can be observed in Fig. 7a–d. Similar images were obtained for the remainder materials. There, it is appreciated the rough surface of the material and the presence of some large pores as well as some voids between micron-sized particles. In the materials heat treated at 800 and 900 °C the microstructure is better revealed as nanoagglomerates, thus enhancing the roughness of the surface.

The TEM images shown in Fig. 7e, f correspond to the CDC sample obtained at 600 °C and containing 5% DVB and reveal the amorphous character of the material, which is also evidenced in the dispersed diffraction rings of the selected area electron diffraction pattern (Fig. 7f). On contrary, by increasing the temperature at 900 °C (Fig. 7g, h), there can be observed some small and poorly crystalized graphitic domains.

Electrochemical characteristics of CDC

Impedance spectroscopy (EIS) data are obtained by applying an AC potential to the electrochemical cell and measuring the current through the cell. The current signal allows determining the impedance of the assembly, and it is usually represented as a Nyquist plot in where is presented the dependence of imaginary vs. real component of impedance, Z'' vs. Z' at different frequencies. The Nyquist plots of the CDC
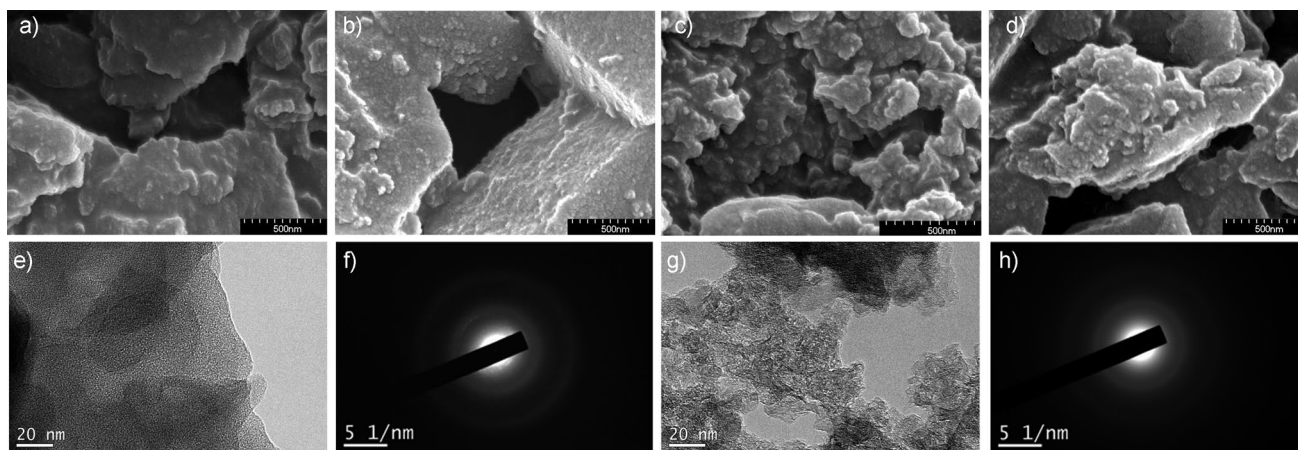
Figure 7 SEM images of the CDC materials containing 5% DVB and chlorinated at **a** 600, **b** 700, **c** 800 and **d** 900 °C. TEM images of CDC materials containing 5% DVB and the corresponding SAED patterns and chlorinated at 600 °C (**e**, **f**) and chlorinated at 900 °C.

materials containing 5% DVB and obtained at different temperatures are collected in Fig. 8a. Similar plots were obtained for the remainder materials. There, it can be appreciated that the increase in the chlorination temperature produces materials with less ohmic resistance (crossing point of the semicircle on the axis of the real impedance). By fitting the high-frequency region to a circuit where a resistor is connected in series to a second parallel circuit, the ohmic resistance, R_s, was determined and is collected in Table 3. In all the cases, the increase in the DVB content leads to a decrease in the R_s.

Although the cyclic voltammetry (CV) and galvanostatic charge and discharge (GCD) experiments are commonly reported in the literature for calculating the capacitance of the CDC materials [46–48], in the case of highly porous carbons, only the low-frequency range of the current (of voltage) can penetrate the narrow and deep pores. At high frequencies, it is then possible to evaluate the non-fractal specific capacitance which avoids the influence of the pores in the electrochemical characteristics of the material. This *true* capacitance (C_{EDL}) can be extracted from the linearization of the CPE (*constant phase element*) formula $\ln\left(Z_{CPE}\right) = \ln\left(Z''\right) = Y_0 - n\ln\left(2\pi f\right)$ by using the Brug–Sluyters' formula [49]:

$$C_{EDL} = Y_0^{1/n}\left(\frac{1}{R_s}\right)^{1-1/n} \tag{4}$$

As it can be observed in Table 3, the C_{EDL} are maintained within a short interval independently on the amount of DVB used to synthesize the ceramer in the

CDC materials obtained at 600 and 700 °C, whereas at the highest chlorination temperatures it is observed a significant decrease in the C_{EDL} values as the DVB content was raised. These capacitance values were further confirmed by GCD experiments (Fig. 8b) from the discharge curves and by using the equation $C_s = I$ $t_d/m \Delta V$ (where I is the current density, t_d is the discharge time in s, m is the mass of the averaged mass of the electrodes, and ΔV is the voltage window, 0.8 V in this case). As predicted there is an increase in the capacitance as increasing the chlorination temperature (Fig. 8c) and the DVB content. Indeed, the most dramatic change occurs in the CDC obtained at 900 °C, where the capacitance increases from 76 to 232 F/g when the DVB content is raised from 1 to 5%. Notice that this increase in the capacitance with the amount of DVB, as determined by GCD measurements, shows the opposite behavior as the capacitances estimated by EIS (Table 3). These discrepancies are attributed to the high microporous character of the materials heat treated at the maximum temperatures (Table 2).

The Ragone plot shown in Fig. 8d represents the energy ($E = C_s \Delta V^2/2 \times 1000/3600$) and power densities ($P = E_d/t_d \times 3600$ of the electrochemical assemblies). Except for the sample obtained at 700 °C and containing 2% DVB, all the remainder materials fall on the same energy and power range. For the sake of clarity, we have extracted from this plot the values of those CDC obtained from ceramers containing 5% DVB and presented separately in Fig. 9. There, it is appreciated that the behavior as potential capacitor electrode is enhanced as the chlorination temperature increases
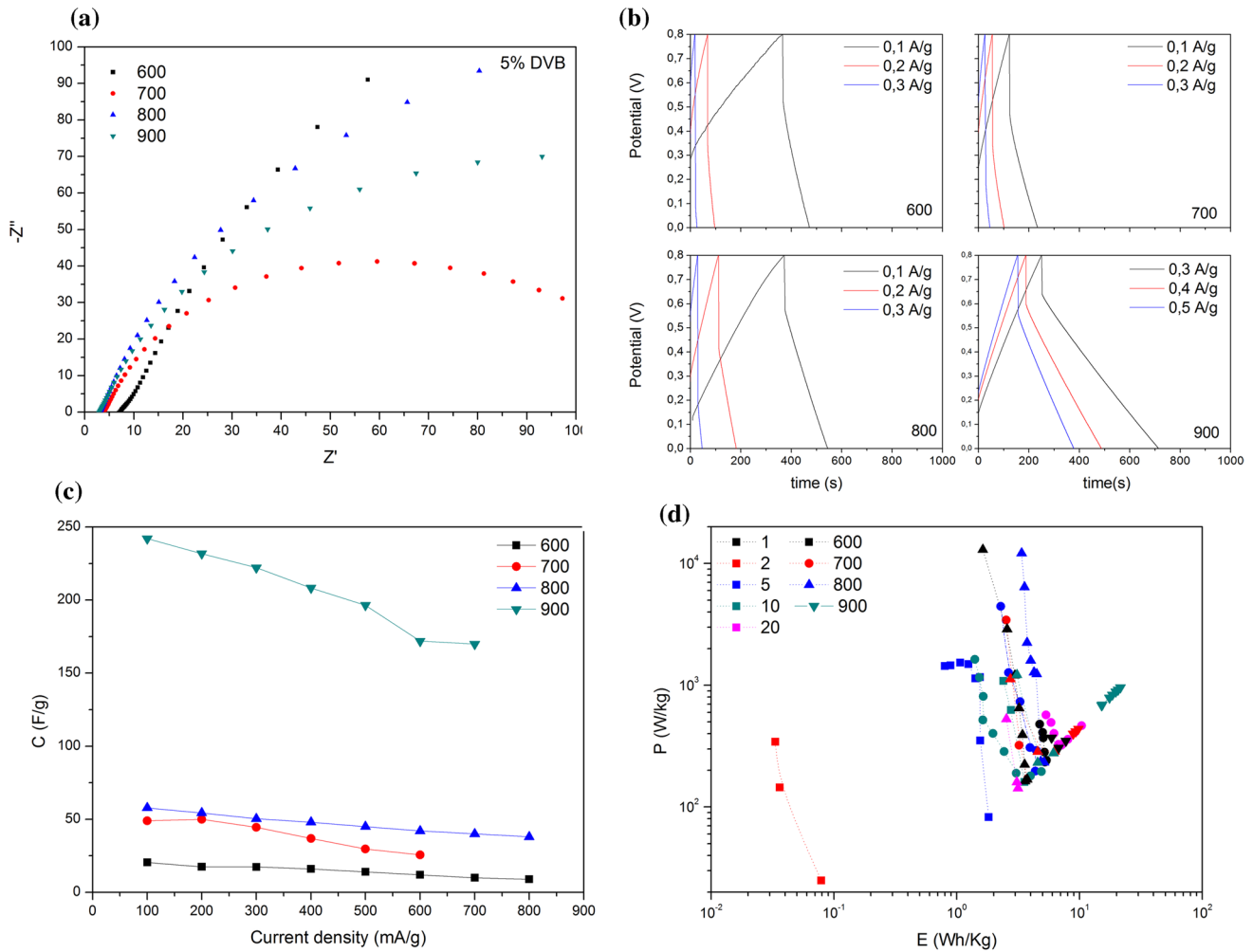
(a)

(b)

(c)

(d)

Figure 8 **a** Nyquist plots of the CDC materials containing 5% DVB, **b** galvanostatic charge and discharge curves of the CDCs containing 5% DVB and obtained at different current densities, **c** capacitance of the same CDC samples at the different current densities, and **d** Ragone plot including the CDC samples prepared at different temperatures and containing different DVB amounts.

(high power and high energy). It is also noticed that the energy span is highly reduced and seem to be independent on the DVB content, whereas the power density can be substantially modified with the DVB amount reaching 10^2 span values, especially in the case of the CDCs obtained at intermediate chlorination temperatures.

Discussion

The carbon enrichment of ceramer materials obtained from AHPCS and DVB has been described since long in many different works [20, 50]. The formation of the carbon during the polymer-to-ceramic conversion occurs in several stages starting by the precipitation of the excess of hydrogenated carbon, and then, the nucleation of the basic structural units takes place followed by the growth of the free carbon clusters via edge-to-edge linkages between adjacent basic structural units. When the temperature is increased, the graphitization of the carbon takes place as well [51]. Some authors demonstrated that increasing the carbon content of the preceramic precursor does not necessarily lead to C-rich ceramics but instead it is the stability of the hydrocarbon linkages whose determine the retaining of the carbon phase [52]. As observed in the FTIR-ATR spectra (Fig. 1b), at low pyrolysis temperature, there is an increase in the number of the less stable dangling

Table 3 Electrochemical characteristics of the CDC materials, as determined by EIS data

% DVB	Temperature (°C)											
	600			700			800			900		
	R_s Ωcm²	C_{EDL} F/g	C_{EDL} F/cm²	R_s Ωcm²	C_{EDL} F/g	C_{EDL} F/cm²	R_s Ωcm²	C_{EDL} F/g	C_{EDL} F/cm²	R_s Ωcm²	C_{EDL} F/g	C_{EDL} F/cm²
1	0.87	45.87	0.67	0.34	28.47	1.21	0.62	500.3	11.25	0.37	119.1	2.84
2	0.81	46.13	0.44	0.30	33.73	1.62	0.30	226.3	9.96	0.28	77.13	1.14
5	0.56	45.69	1.06	0.31	28.67	1.39	0.25	83.35	1.14	0.24	26.81	0.47
10	0.35	38.82	0.61	0.25	35.93	1.58	0.28	43.95	2.26	0.18	58.24	0.88
20	0.32	41.98	1.33	0.24	14.33	1.42	0.24	25.55	2.70	0.18	55.84	1.00

Figure 9 Ragone plot of the CDC materials obtained from ceramers containing 5% DVB and chlorinated at different temperatures.

bonds in the SiC structure when the DVB content in the preceramic material is increased. This fact leads to a small amount of free carbon domains (as deduced from the Raman spectrum in Fig. 2). In this first stage of carbon formation, there are formed some basic structural units in the form of graphene layers due to the nucleation of some aromatic rings from the DVB molecules.

Achieving a good cross-linked ratio is feasible by adjusting the amount of DVB with respect to the polycarbosilane, since the steric hindrance produced by the high benzyl group in the DVB leads to a reduction in the evolution of the hydrosilylation reaction [20]. In addition, DVB molecules also react with each other and not only with the AHPCS during the cross-linking process [22]. In the FTIR-ATR spectra, there was observed the expected decrease in the Si–H bond as the DVB content was increased (Fig. 1) which accordingly to Bouillon et al. [52] an increase in the carbon content should be expected. Large amounts of amorphous carbon in C-rich PDC were encountered by Dalcanale et al. who demonstrated that, after the incorporation of DVB to a PCS matrix, there exists a considerable increase in the free carbon content, but mainly in the form of amorphous carbon [50].

Indeed, in the thermal analysis (Fig. 3), there is observed that the extent of the exothermic reaction due to the oxidation of the carbon increases with the DVB content but the temperature at which this

reaction takes place is not modified thus suggesting that the structural features of this carbon phase remain at this temperature independently of the initial carbon content. On contrary, by increasing the pyrolysis temperature, it is observed that the oxidative carbon reaction is shifted to higher temperature (Fig. 3) and even at the highest amount of DVB and temperatures, the decomposition takes place in several stages indicating different forms of carbon. The same conclusion arises when analyzing the thermal decomposition in inert atmosphere. At low DVB contents, the carbon domains possess similar thermal (structural) characteristics independently on the pyrolysis temperature, but the increase in the DVB content leads to more thermically stable structures but with major predisposition to subsequent rearrangements.

The decreased amount of Si remaining in the CDC as both the DVB content and the pyrolysis temperature increase (Table 1) is in perfect agreement with the exothermic peaks observed in the thermal analysis carried out in oxidant atmosphere in the sense that the Si that is more susceptible to be etched away by the Cl_2 is the inorganic Si, either in the form of Si or SiO_2. In the formation of the CDC not only the chlorination temperature determines the morphology and crystallinity of the carbon domains but also the hydrogen content. As Choi et al. [53] reported, the presence of H decreases the growth rate of the carbon because of the reaction of the chlorine atoms with H to form HCl. This fact should be the responsible of the decrease in the calculated L_a value of the samples obtained at 600 °C as the DVB content increases whereas at the remainder chlorination temperatures, the size of the graphene layers (La) in the CDC increases as the synthesis temperature does. Notice that the formula used to calculate the La value is assumed to valid for $La < 2$ nm, however, as observed in Fig. 4b, the calculated La values are slightly higher than 2 nm. Some studies point out that the sp^3 carbon atoms act as linkers between small graphene platelets which dominate the structure of the carbide-derived carbons which evolve to large graphitic domains as the chlorination temperature increases [54]. In the XRD patterns (Fig. 5), there were observed two broad bands and a sharp peak attributed to the small carbon crystallites. Coinciding with the Raman results, there were observed a slight increase in the L_c value as the chlorination temperature increases but in any case, this lateral crystallite size exceeds 2 nm.

Below 1000 °C, the CDC obtained from SiC is not sufficiently graphitized, thus producing an amorphous and disordered structure composed of nonplanar carbon structures including pentagonal and heptagonal rings [55]. Indeed, chlorination studies of binary and ternary carbides at low temperature suggest that at such temperatures, there might exist some carbon rings with orders different than six [54, 56]. In the Raman spectrum, it should be taken into account that the G mode exclusively accounts on the in-plane bond-stretching motion of pairs of C sp^2 bonded atoms, whereas the D-peak is associated with the distribution of sp^2 bonded clusters with different ring sizes. The presence of different order in rings tends to decrease the peak height and increase the width. Based on these considerations, the authors highlight that these La values should be taken with extreme care.

There exist significant differences in the graphitization degree of the CDC obtained from different SiC allotropes. Graphene stacking is more favorable when the CDC is obtained from β-SiC leading to higher crystalline graphite than when the CDCs are obtained from α-SiC which produce very short-range-ordered structures enriched in sp^3-bonded carbon and nanoscale graphitic domains [57]. In fact, Urbonaite et al. [58] reported that the average in-plane correlation length (La) of CDC obtained from different carbides is independent on the chlorination temperature but strongly depends on the carbide precursor. In our materials, the absence of any correlation between the I_{2D}/I_G ratio (Fig. 4c) and the La values therefore confirm that the stacks of graphene layers in the CDC materials must be significantly curved [59]. The high curvature of these graphene layers was perfectly appreciated in the TEM images (Fig. 7). These curved structures are highly avid for chlorine so, in addition to the chemical etching of the ceramer structure, the precipitated amorphous carbon must also react with the adsorbed chlorine forming graphitic-like nanoribbons, as previously reported [29].

The equivalent series resistances of the CDC as calculated from EIS experiments decrease as the DVB content increases in the material, and the highest values were encountered in the materials heat treated at 600 °C. Considering the total area of the electrode, these values range from 0.87 to 0.32 $Ωcm^2$ in the samples chlorinated at the lowest temperatures and reach values as low as 0.18 $Ωcm^2$ when the CDC was obtained at 900 °C. This intrinsic resistance (ESR) is even lower than the most common values encountered

in the literature, being in the range of 0.25–0.3 Ωcm^2 for ordered mesoporous SiC-derived carbons and TiC-derived carbons [60, 61]. When the CDC materials were obtained from an oxygenated carbide source, the ESR increases significantly which in turn lowers the energy density and power density values, as occurs in the CDC materials obtained at the lowest temperatures (Fig. 7) [62, 63].

The intrinsic areal capacitance as calculated from the EIS measurements acquired the maximum values in the sample heat treated at 800 °C and containing the lowest amount of DVB but then, this value drops significantly when the DVB content was raised. These values are quite high compared to the literature for aqueous electrolytes [60, 64]. However, the gravimetric capacitance for this sample is maintained in a range between 70 and 50 F/g (Fig. 6), which is a typical value of CDCs obtained at low temperature [65]. These differences in the areal and gravimetric capacitances are attributed to the high anisotropy of the pores and the micropore content (Fig. 5; Table 2). As Zheng et al.[66] proposed, the presence of micropores improves the material capacity; however, in the occurrence of adjacent ion layers, there might be a reduction of the accessible surface area, and thus, the micropores are not fully utilized, then leading to an overall decrease in the gravimetric capacitance (Figs. 8, 9).

By increasing the temperature, the gravimetric capacitance increases as well as the energy of the device. In the material heat treated at 900 °C, it is found a high amount of micropores as well as high pore anisotropy; however, the differences in the gravimetric and specific capacitances are reduced in a significant amount. The gravimetric capacitance of the CDC chlorinated at 900 °C reaches values as high as 232 F/g at 100 mA/g as in carbon-enriched nano-CDC [67]. These values are similar to the ones encountered by Mazo et al. in fluorine-doped CDC obtained from silicon oxycarbide materials [68]. These authors demonstrated that during the etching process, fluorine atoms were incorporated into the silicon oxycarbide network forming both SiO -F bonds and both C–F semi-ionic and C–F covalent bonds, thus increasing the wettability of the electrodes and promoting Faradaic processes [68]. The presence of F – Si bond and no C – F bond were also reported by Xia et al. [69] in N-doped silicon oxycarbide-derived carbons with capacitance values of 272 F/g at the current density of 0.2 A/g in 6 M KOH aqueous electrolyte [69]. In both cases, the temperatures of the treatments are

comprised between 1000 and 1400 °C, significantly higher than in our material samples, with the concurrent cost increase.

Contrary to what occurs in the samples obtained at 600–800 °C, the Ragone plot of the optimized materials (those obtained at 900 °C) shows also no variations in the energy and power provided by the device with the different DVB amounts despite of the different capacitance values. In these materials, the double layer should be highly accessible to the electrolyte although the pore anisotropy is quite high and the micropore content also reaches percentage values over 90%. This conclusion is extracted from the ESR values calculated from the EIS experiments, which are, by far, lower than in other CDCs [60–63]. The reported power density for CDCs obtained from AHPCS doped with Co atoms and heat treated within the studied temperature range is 160–285 W/kg and the energy density vales were 0.6–1 W h/kg, depending upon the temperature of the treatment [70]. In this work, the power density values fall around 600–1000 W/kg, slightly higher than the values reported for mesoporous carbons 98–782 W/kg [71]. The energy values, on contrary, are about 20 W h/kg, which is still higher compared to the 0.6–1 W h/kg encountered for the referred carbon materials [71]. Thus, by treating the PDC at 900 °C it has been reached an optimized surface where the capacitance depends on the amount of extra C incorporated, thus allowing designing an electrochemical device throwing the maximum power at the lowest energy demand.

Conclusions

Polymer-derived ceramics are an excellent strategy solution to obtain carbide-derived carbons with tunable morphologies and structures. In this work, it has been demonstrated that not only incorporating carbon into the preceramic structure is a necessary condition to achieve good capacitance values but also, this carbon should be somehow incorporated into the ceramic structure by forming carbidic-like environments. At low temperatures, the excess carbon precipitates as amorphous carbon which during chlorination suffers minimal variations thus not enhancing the capacitive properties of the resulting material. By increasing the pyrolysis temperature, there are more Si–C bindings which in turn results in a better performance as capacitor electrodes. Despite that the capacitance increases significantly with the amount of DVB incorporated,

the power/energy ratio is independent on the amount of DVB incorporated, a result which is attributed to the highly microporous character of the sample and the large pore anisotropy as well.

Author contributions

Aitana Tamayo contributed to conceptualization, methodology, project administration, writing—original draft preparation, and writing—review and editing. Mª Angeles Rodriguez was involved in investigation. Juan Rubio contributed to project administration and supervision. Fausto Rubio was involved in investigation, funding acquisition, and original draft reviewing and provided software.

Data and code availability

Not applicable.

Declarations

Conflicts of interest There are no conflicts of interest to declare.

Ethical approval Not applicable.

References

[1] Díez Nogués N, Sevilla Solís M, Fuertes Arias AB (2021) Synthesis strategies of templated porous carbons beyond the silica nanocasting technique. Carbon 178:451–476

[2] Gu WT, Yushin G (2014) Review of nanostructured carbon materials for electrochemical capacitor applications: advantages and limitations of activated carbon, carbide-derived carbon, zeolite-templated carbon, carbon aerogels, carbon nanotubes, onion-like carbon, and graphene. Wiley Interdiscipl Rev-Energy Environ 3:424–473

[3] Li J-G, Ho Y-F, Ahmed MMM, Liang H-C, Kuo S-W (2019) Mesoporous carbons templated by PEO-PCL block copolymers as electrode materials for supercapacitors. Chem—A Eur J 25:10456–10463

[4] Salunkhe RR, Kaneti YV, Kim J, Kim JH, Yamauchi Y (2016) Nanoarchitectures for metal-organic framework-derived nanoporous carbons toward supercapacitor applications. Acc Chem Res 49:2796–2806

[5] Zhou J-E, Chen J, Peng Y, Zheng Y, Zeb A, Lin X (2022) Metal-organic framework-derived transition metal sulfides and their composites for alkali-ion batteries: a review. Coord Chem Rev 472:214781

[6] Gogotsi Y, Nikitin A, Ye H et al (2003) Nanoporous carbide-derived carbon with tunable pore size. Nat Mater 2:591–594

[7] Ratajczak P, Suss ME, Kaasik F, Beguin F (2019) Carbon electrodes for capacitive technologies. Energy Storage Mater 16:126–145

[8] Chen XY, Song H, Zhang ZJ, He YY (2014) A rational template carbonization method for producing highly porous carbon for supercapacitor application. Electrochim Acta 117:55–61

[9] Merlet C, Rotenberg B, Madden PA et al (2012) On the molecular origin of supercapacitance in nanoporous carbon electrodes. Nat Mater 11:306–310

[10] Krawiec P, Schrage C, Kockrick E, Kaskel S (2008) Tubular and rodlike ordered mesoporous silicon (Oxy)carbide ceramics and their structural transformations. Chem Mater 20:5421–5433

[11] Dyjak S, Kiciński W, Norek M, Dyjak M, Cudziło S (2019) Carbide-derived carbon obtained via bromination of titanium carbide: Comparative analysis with chlorination and hydrogen storage studies. Microporous Mesoporous Mater 273:26–34

[12] Presser V, Heon M, Gogotsi Y (2011) Carbide-derived carbons–from porous networks to nanotubes and graphene. Adv Func Mater 21:810–833

[13] Dash R, Yushin G, Gogotsi Y (2005) Synthesis, structure and porosity analysis of microporous and mesoporous carbon derived from zirconium carbide. Microporous Mesoporous Mater 86:50–57

[14] Duan L, Ma Q, Dai X et al (2015) The effect of etching temperature on the compositional and structural evolution of ceramer from polysiloxane in chlorine. Corros Sci 101:132–138

[15] Käärik M, Arulepp M, Kook M et al (2018) Characterisation of steam-treated nanoporous carbide-derived carbon of TiC origin: structure and enhanced electrochemical performance. J Porous Mater 25:1057–1070

[16] Dyatkin B, Mamontov E, Cook KM, Gogotsi Y (2015) Capacitance, charge dynamics, and electrolyte-surface interactions in functionalized carbide-derived carbon electrodes. Progr Nat Sci: Mater Int 25:631–641

[17] Lale A, Schmidt M, Mallmann MD et al (2018) Polymer-Derived ceramics with engineered mesoporosity: from design to application in catalysis. Surf Coat Technol 350:569–586

[18] Maddocks AR, Cassidy DJ, Jones AS, Harris AT (2009) Synthesis of nanoporous silicon carbide via the preceramic polymer route. Mater Chem Phys 113:861–867

[19] Tolosa A, Krüner B, Jäckel N, Aslan M, Vakifahmetoglu C, Presser V (2016) Electrospinning and electrospraying of silicon oxycarbide-derived nanoporous carbon for supercapacitor electrodes. J Power Sour 313:178–188

[20] Maddocks AR, Hook JM, Stender H, Harris AT (2008) Heterogeneously catalysed crosslinking of polycarbosilane with divinylbenzene. J Mater Sci 43:2666–2674

[21] Li Z, Wang Y, An L (2017) Control of the thermal conductivity of SiC by modifying the polymer precursor. J Eur Ceram Soc 37:61–67

[22] Drechsel C, Peterlik H, Gierl-Mayer C, Stöger-Pollach M, Konegger T (2021) Influence of DVB as linker molecule on the micropore formation in polymer-derived SiCN ceramics. J Eur Ceram Soc 41:3292–3302

[23] Duan L, Ma Q, Chen Z (2014) Etching process of silicon carbide from polysiloxane by chlorine. Corros Sci 87:127–133

[24] Duan L, Ma Q, Chen Z (2015) Fabrication and CO2 capture performance of silicon carbide derived carbons from polysiloxane. Microporous Mesoporous Mater 203:24–31

[25] Zheng K, Zou X, Xie X, Lu C, Li S, Lu X (2018) Electrosynthesis of SiC derived porous carbon nanospheres for supercapacitors. Mater Lett 216:265–268

[26] Guo M, Chen X, Zhang X et al (2019) Molten alkaline synthesis of highly porous carbon from calcium carbide. Microporous Mesoporous Mater 278:397–402

[27] Oschatz M, Kockrick E, Rose M et al (2010) A cubic ordered, mesoporous carbide-derived carbon for gas and energy storage applications. Carbon 48:3987–3992

[28] Oschatz M, Zeiger M, Jäckel N et al (2015) Emulsion soft templating of carbide-derived carbon nanospheres with controllable porosity for capacitive electrochemical energy storage. J Mater Chem A 3:17983–17990

[29] Perez-Roman B, Layek R, Rodriguez M, Rubio F, Rubio J, Tamayo A (2021) Insights into the structural and surface characteristics of microporous carbide derived carbons obtained through single and double halogen etching. Microporous Mesoporous Mater 310:110675

[30] Soraru GD, Campostrini R, Ejigu AA, Zera E, Jana P (2016) Processing and characterization of polymer derived SiOC foam with hierarchical porosity by HF etching. J Ceram Soc Jpn 124:1023–1029

[31] Hasegawa Y (1989) Synthesis of continuous silicon carbide fibre. J Mater Sci 24:1177–1190

[32] Kaneko T, Nemoto D, Horiguchi A, Miyakawa N (2005) FTIR analysis of a-SiC: H films grown by plasma enhanced CVD. J Cryst Growth 275:e1097–e1101

[33] Wolfe D, Hinds B, Wang F et al (1999) Thermochemical stability of silicon–oxygen–carbon alloy thin films: a model system for chemical and structural relaxation at SiC–SiO 2 interfaces. J Vac Sci Technol, A: Vac, Surf Films 17:2170–2177

[34] Ferrari AC (2007) Raman spectroscopy of graphene and graphite: disorder, electron–phonon coupling, doping and nonadiabatic effects. Solid State Commun 143:47–57

[35] Claramunt S, Varea A, Lopez-Diaz D, Velázquez MM, Cornet A, Cirera A (2015) The importance of interbands on the interpretation of the Raman spectrum of graphene oxide. J Phys Chem C 119:10123–10129

[36] Saito R, Jorio A, Souza Filho AG, Dresselhaus G, Dresselhaus M, Pimenta MA (2001) Probing phonon dispersion relations of graphite by double resonance Raman scattering. Phys Rev Lett 88:027401

[37] Fantini C, Pimenta MA, Strano MS (2008) Two-Phonon Combination Raman modes in covalently functionalized single-wall carbon nanotubes. J Phys Chem C 112:13150–13155

[38] Ferrari AC (2007) Raman spectroscopy of graphene and graphite: disorder, electron-phonon coupling, doping and nonadiabatic effects. Solid State Commun 143:47–57

[39] Zickler GA, Smarsly B, Gierlinger N, Peterlik H, Paris O (2006) A reconsideration of the relationship between the crystallite size La of carbons determined by X-ray diffraction and Raman spectroscopy. Carbon 44:3239–3246

[40] Fujimoto H (2003) Theoretical X-ray scattering intensity of carbons with turbostratic stacking and AB stacking structures. Carbon 41:1585–1592

[41] Scherrer P (1918) Bestimmung der Grosse und inneren Struktur von Kolloidteilchen mittels Rontgenstrahlen. Nach Ges Wiss Gottingen 2:8–100

[42] Rouquerol J, Llewellyn P, Rouquerol F (2007) Is the BET equation applicable to microporous adsorbents. Stud Surf Sci Catal 160:49–56

[43] Thommes M, Kaneko K, Neimark AV et al (2015) Physisorption of gases, with special reference to the evaluation of surface area and pore size distribution (IUPAC Technical Report). Pure Appl Chem 87:1051–1069

[44] Lippens BC, De Boer J (1965) Studies on pore systems in catalysts: V: The t Method. J Catal 4:319–323

[45] Pomonis PJ, Armatas GS (2004) A method for the estimation of pore anisotropy in porous solids. Langmuir 20:6719–6726

[46] Shen H-H, Hu C-C (2014) Capacitance enhancement of activated carbon modified in the propylene carbonate electrolyte. J Electrochem Soc 161:A1828

[47] Jurewicz K, Vix-Guterl C, Frackowiak E et al (2004) Capacitance properties of ordered porous carbon materials prepared by a templating procedure. J Phys Chem Solids 65:287–293

[48] Kwon HC, Choi S, Wang Y, Othman R, Choi M (2020) Scalable synthesis of zeolite-templated ordered microporous carbons without external carbon deposition for capacitive energy storage. Microporous Mesoporous Mater 307:110481

[49] Brug G, van den Eeden AL, Sluyters-Rehbach M, Sluyters JH (1984) The analysis of electrode impedances complicated by the presence of a constant phase element. J Electroanal Chem Interfac Electrochem 176:275–295

[50] Dalcanale F, Grossenbacher J, Blugan G et al (2014) Influence of carbon enrichment on electrical conductivity and processing of polycarbosilane derived ceramic for MEMS applications. J Eur Ceram Soc 34:3559–3570

[51] Wen Q, Yu Z, Riedel R (2020) The fate and role of in situ formed carbon in polymer-derived ceramics. Prog Mater Sci 109:100623

[52] Bouillon E, Pailler R, Naslain R et al (1991) New poly(carbosilane) models. 5. Pyrolysis of a series of functional poly(carbosilanes). Chem Mater 3:356–367

[53] Choi H-J, Bae H-T, McNallan MJ, Sohn Y-H, Lim D-S (2009) Effect of hydrogen on the physical and mechanical properties of silicon carbide-derived carbon films. Surf Coat Technol 204:1018–1021

[54] de Tomas C, Suarez-Martinez I, Marks NA (2018) Carbide-derived carbons for dense and tunable 3D graphene networks. Appl Phys Lett 112:251907

[55] Welz S, McNallan MJ, Gogotsi Y (2006) Carbon structures in silicon carbide derived carbon. J Mater Process Technol 179:11–22

[56] Bae J-S, Nguyen TX, Bhatia SK (2014) Pore accessibility of Ti3SiC2-derived carbons. Carbon 68:531–541

[57] Jeong MG, Yoon SH, Chun YS, Lee ES, Lim D-S (2014) Effect of lattice structure of silicon carbide on crystal formation of carbide-derived carbon. Carbon 79:19–27

[58] Urbonaite S, Hälldahl L, Svensson G (2008) Raman spectroscopy studies of carbide derived carbons. Carbon 46:1942–1947

[59] Käärik M, Arulepp M, Karelson M, Leis J (2008) The effect of graphitization catalyst on the structure and porosity of SiC derived carbons. Carbon 46:1579–1587

[60] Tsai W-Y, Gao P-C, Daffos B et al (2013) Ordered mesoporous silicon carbide-derived carbon for high-power supercapacitors. Electrochem Commun 34:109–112

[61] Pérez CR, Yeon SH, Ségalini J et al (2013) Structure and electrochemical performance of carbide-derived carbon nanopowders. Adv Func Mater 23:1081–1089

[62] Gao P-C, Tsai W-Y, Daffos B et al (2015) Graphene-like carbide derived carbon for high-power supercapacitors. Nano Energy 12:197–206

[63] Krüner B, Odenwald C, Tolosa A et al (2017) Carbide-derived carbon beads with tunable nanopores from continuously produced polysilsesquioxanes for supercapacitor electrodes. Sustain Energy Fuels 1:1588–1600

[64] Patel KK, Singhal T, Pandey V, Sumangala TP, Sreekanth MS (2021) Evolution and recent developments of high performance electrode material for supercapacitors: a review. J Energy Storage 44:103366

[65] Wu H, Wang X, Jiang L et al (2013) The effects of electrolyte on the supercapacitive performance of activated calcium carbide-derived carbon. J Power Sour 226:202–209

[66] Zheng Y, Deng T, Zhang W, Zheng W (2020) Optimizing the micropore-to-mesopore ratio of carbon-fiber-cloth creates record-high specific capacitance. J Energy Chem 47:210–216

[67] Alhabeb M, Beidaghi M, Van Aken KL, Dyatkin B, Gogotsi Y (2017) High-density freestanding graphene/carbide-derived carbon film electrodes for electrochemical capacitors. Carbon 118:642–649

[68] Mazo MA, Colomer MT, Tamayo A, Rubio J (2022) Hierarchical porous fluorine-doped silicon oxycarbide derived materials: physicochemical characterization and electrochemical behaviour. Microporous Mesoporous Mater 330:111604

[69] Xia K, Cheng Y, Zhang H, Han F, Duan L, Liu X (2023) Highly microporous nitrogen-doped carbon derived from silicon oxycarbide ceramics for supercapacitor application. J Inorg Organometal Polym Mater 33(7):1–12

[70] Tamayo A, Rodriguez MA, Rubio F, Rubio J (2022) Cobalt catalyzed tunable carbon microstructures from halogenated SiC preceramic precursors. J Am Ceram Soc. https://doi.org/10.1111/jace.18436

[71] Prabaharan SRS, Vimala R, Zainal Z (2006) Nanostructured mesoporous carbon as electrodes for supercapacitors. J Power Sour 161:730–736